BEND-FLOW SIMULATION USING 2D DEPTH-AVERAGED MODEL

By H. C. Lien,[1] T. Y. Hsieh,[2] J. C. Yang,[3] Member, ASCE, and K. C. Yeh,[4] Associate Member, ASCE

ABSTRACT: The purpose of this paper is to present a 2D depth-averaged model for simulating and examining flow patterns in channel bends. In particular, this paper proposes a 2D depth-averaged model that takes into account the influence of the secondary flow phenomenon through the calculation of the dispersion stresses arisen from the integration of the products of the discrepancy between the mean and the true velocity distributions. The proposed model uses an orthogonal curvilinear coordinate system to efficiently and accurately simulate the flow field with irregular boundaries. As for the numerical solution procedure, the two-step split-operator approach consisting of the dispersion step and the propagation step with the staggered grid is used to numerically solve the flow governing equations. Two sets of experimental data from de Vriend and Koch and from Rozovskii were used to demonstrate the model's capabilities. The former data set was from a mildly curved channel, whereas the latter was from a sharply curved channel. The simulations considering the secondary flow effect agree well with the measured data. Furthermore, an examination of the dispersion stress terms shows that the dispersion stresses play a major role in the transverse convection of the momentum shifting from the inner bank to the outer bank for flows in both mild and sharp bends.

INTRODUCTION

Flow characteristics in channel bends are much more complicated than those in straight reaches. The occurrence of the secondary flow is one of the dominant features of flows in bends. Secondary flow results from the imbalance between the transverse water surface gradient force and centrifugal force over the depth due to the vertical variation of the primary flow velocity. In other words, the inward pressure gradient near the bed prevails over the centrifugal force resulting in an inward flow along the bed and an outward flow near the water surface. This circulatory flow pattern is termed secondary flow. Pioneering investigations of the flow phenomena in open-channel bends are generally attributed to Thompson (1876) who observed the spiral motion inherent in a channel bend by introducing seeds and dyes into the flow. Since then, many studies have been conducted on flows in bends [e.g., Mockmore (1943), Shukhry (1949), Rozovskii (1961), and Yen (1965)].

The 3D numerical models have been developed (Leschziner and Rodi 1979; Shimizu et al. 1990; Sinha et al. 1998) to simulate the complicated spiral flow motion in the bend. However, 2D depth-averaged models are often adopted in practice by hydraulic engineers because of their easy implementation and application. For 2D bend-flow models, steady-flow models, such as that of Odgaard (1989), have been developed to avoid the possible numerical instability and large amount of computation time. After reviewing both laboratory and field data obtained by others (de Vriend and Geldof 1983; Kikkawa et al. 1976; Zimmermann and Kennedy 1978), Odgaard (1989) found that both the velocity and flow depth are essentially constant along the river channel's centerline and that their variation in the transverse direction is nearly linear over the central portion of the cross section. Hence, the velocity and flow depth in the lateral direction are linearized with respect to their centerline values in Odgaard's model. Yen and Ho (1990) developed a numerical model for the simulation of bed evolution in channel bends with fixed walls. They followed Odgaard's concept and adopted several published approximations of the transverse velocity distribution to reduce the depth-averaged water flow equations. An alternative approach for describing bend flow is to use the concept of moment of momentum (Falcon Ascanio 1979; Jin and Steffler 1993; Yeh and Kennedy 1993). The method couples the depth-averaged continuity and momentum equations with two moment-of-momentum equations derived from the balance among the momentum flux of the convective terms, pressure gradient term, and stress terms for closure purposes. For steady bend-flow models, the determination of flow depth in the flow domain is difficult due to the lack of time derivative of the flow depth in the continuity equation. Hence, the flow depth cannot be calculated directly from the differential continuity equation. Generally speaking, in steady-flow models the flow depth at the centerline can first be computed through the integration of discharge over the cross section; then its profile in the transverse direction is linearized with respect to the centerline value (Odgaard 1989; Yen and Ho 1990), or computed by the method of integration (Kalkwijk and de Vriend 1980).

Among the existing unsteady 2D bend-flow models, the models developed by Molls and Chaudhry (1995) and Nagata et al. (1997) are discussed in this paper. Molls and Chaudhry's model (1995) simulated the experimental bend-flow data conducted by Rozovskii (1961). They proposed the concept of integrated effective stress, which consists of laminar viscosity stress, turbulence stress, and dispersion stress due to depth-averaging. However, they ignored the nonuniform distribution of vertical velocity in the bend-flow simulation. Nagata et al.'s model (1997) considers a secondary flow component that was derived by using the vertical distributions of the main and transverse velocities in the same way as Kalkwijk and de Vriend (1980). In their studies, only one of the dispersion stresses acting on the face perpendicular to the streamwise axis and acting in the direction of the transverse axis is used as the secondary flow component.

The dispersion stress terms resulted from the integration of the product of the difference between the mean velocity and the true velocity distribution in the bend-flow field. de Vriend (1977) used the perturbation method to derive the velocity distribution over the depth in the shallow curved channel, and the vertical velocity profiles were then verified by the experiments. The vertical velocity distribution of the main flow and

[1]PhD Candidate, Dept. of Civ. Engrg., Nat. Chiao Tung Univ., 1001 Ta Hsueh Rd., Hsinchu, 30050 Taiwan. E-mail: u8116541@cc.nctu.edu.tw

[2]Grad. Student, Dept. of Civ. Engrg., Nat. Chiao Tung Univ., 1001 Ta Hsueh Rd., Hsinchu, 30050 Taiwan.

[3]Prof., Dept. of Civ. Engrg., Nat. Chiao Tung Univ., 1001 Ta Hsueh Rd., Hsinchu, 30050 Taiwan.

[4]Prof., Dept. of Civ. Engrg., Nat. Chiao Tung Univ., 1001 Ta Hsueh Rd., Hsinchu, 30050 Taiwan.

Note: Discussion open until March 1, 2000. To extend the closing date one month, a written request must be filed with the ASCE Manager of Journals. The manuscript for this paper was submitted for review and possible publication on March 20, 1998. This paper is part of the ***Journal of Hydraulic Engineering***, Vol. 125, No. 10, October, 1999. ©ASCE, ISSN 0733-9429/99/0010-1097–1108/$8.00 + $.50 per page. Paper No. 17977.

J. Hydraul. Eng. 1999.125:1097-1108.

secondary flow can be approximated by a logarithmic profile and a nonlinear profile, respectively. Using these velocity distributions, one can obtain the dispersion stresses by numerical integration.

The purpose of this paper is to present an unsteady 2D depth-averaged flow model with the consideration of dispersion stress terms to simulate the bend-flow field. The model uses an orthogonal curvilinear coordinate system to efficiently and accurately simulate the flow field with irregular boundaries. Numerically, the proposed model applies a two-step split-operator approach proposed by Lien et al. (1999) for solving the flow governing equations. Two sets of experimental data measured by de Vriend and Koch (1977) and Rozovskii (1961) are used to examine the capabilities of the proposed model in simulating the bend flow.

MATHEMATICAL FORMULATION

Depth-Averaged Equations in Orthogonal Curvilinear Coordinates

Under the assumption of incompressible fluid, constant viscosity, and a hydrostatic pressure distribution over the depth, the depth-averaged equations can be obtained from integrating Navier-Stokes equations from the channel bottom to the water surface with the kinematic boundary conditions. The unsteady 2D depth-averaged flow governing equations including the basic continuity and momentum equations can, respectively, be written in orthogonal curvilinear coordinates as follows:

Continuity equation

$$h_1 h_2 \frac{\partial d}{\partial t} + \frac{\partial}{\partial \xi}(h_2 \bar{\bar{u}} d) + \frac{\partial}{\partial \eta}(h_1 \bar{\bar{v}} d) = 0 \tag{1}$$

Momentum equations

ξ-direction

$$\begin{aligned}
&\frac{\partial \bar{\bar{u}}}{\partial t} + \frac{\bar{\bar{u}}}{h_1}\frac{\partial \bar{\bar{u}}}{\partial \xi} + \frac{\bar{\bar{v}}}{h_2}\frac{\partial \bar{\bar{u}}}{\partial \eta} + \frac{1}{h_1 h_2}\frac{\partial h_1}{\partial \eta}\overline{\bar{u}\bar{v}} - \frac{1}{h_1 h_2}\frac{\partial h_2}{\partial \xi}\overline{\bar{v}^2} \\
&= -\frac{g}{h_1}\frac{\partial}{\partial \xi}(z_b + d) + \frac{1}{\rho h_1 h_2 d}\frac{\partial}{\partial \xi}(h_2 T_{11}) + \frac{1}{\rho h_1 h_2 d}\frac{\partial}{\partial \eta}(h_1 T_{12}) \\
&+ \frac{1}{\rho h_1 h_2 d}\frac{\partial h_1}{\partial \eta} T_{12} - \frac{1}{\rho h_1 h_2 d}\frac{\partial h_2}{\partial \xi} T_{22} + \frac{\tau_{s_1} - \tau_{b_1}}{\rho d} \\
&+ \frac{1}{\rho h_1 h_2 d}\left[-(h_2\tau_{11})_s \frac{\partial z_s}{\partial \xi} + (h_2\tau_{11})_b \frac{\partial z_b}{\partial \xi} - (h_1\tau_{12})_s \frac{\partial z_s}{\partial \eta} \right. \\
&\left. + (h_1\tau_{12})_b \frac{\partial z_b}{\partial \eta}\right]
\end{aligned} \tag{2}$$

η-direction

$$\begin{aligned}
&\frac{\partial \bar{\bar{v}}}{\partial t} + \frac{\bar{\bar{u}}}{h_1}\frac{\partial \bar{\bar{v}}}{\partial \xi} + \frac{\bar{\bar{v}}}{h_2}\frac{\partial \bar{\bar{v}}}{\partial \eta} + \frac{1}{h_1 h_2}\frac{\partial h_2}{\partial \xi}\overline{\bar{u}\bar{v}} - \frac{1}{h_1 h_2}\frac{\partial h_1}{\partial \eta}\overline{\bar{u}^2} \\
&= -\frac{g}{h_2}\frac{\partial}{\partial \eta}(z_b + d) + \frac{1}{\rho h_1 h_2 d}\frac{\partial}{\partial \xi}(h_2 T_{12}) + \frac{1}{\rho h_1 h_2 d}\frac{\partial}{\partial \eta}(h_1 T_{22}) \\
&- \frac{1}{\rho h_1 h_2 d}\frac{\partial h_1}{\partial \eta} T_{11} + \frac{1}{\rho h_1 h_2 d}\frac{\partial h_2}{\partial \xi} T_{12} + \frac{\tau_{s_2} - \tau_{b_2}}{\rho d} \\
&+ \frac{1}{\rho h_1 h_2 d}\left[-(h_2\tau_{12})_s \frac{\partial z_s}{\partial \xi} + (h_2\tau_{12})_b \frac{\partial z_b}{\partial \xi} - (h_1\tau_{22})_s \frac{\partial z_s}{\partial \eta} \right. \\
&\left. + (h_1\tau_{22})_b \frac{\partial z_b}{\partial \eta}\right]
\end{aligned} \tag{3}$$

in which

$$T_{11} = \int_{z_b}^{z_s} [\tau_{11} - \rho\overline{u'^2} - \rho(\bar{u} - \bar{\bar{u}})^2]\, dz \tag{4}$$

$$T_{22} = \int_{z_b}^{z_s} [\tau_{22} - \rho\overline{v'^2} - \rho(\bar{v} - \bar{\bar{v}})^2]\, dz \tag{5}$$

$$T_{12} = T_{21} = \int_{z_b}^{z_s} [\tau_{12} - \rho\overline{u'v'} - \rho(\bar{u} - \bar{\bar{u}})(\bar{v} - \bar{\bar{v}})\, dz \tag{6}$$

$$\frac{\tau_{11}}{\rho} = 2\nu_l \left[\frac{1}{h_1}\frac{\partial \bar{u}}{\partial \xi} + \frac{\bar{v}}{h_1 h_2}\frac{\partial h_1}{\partial \eta}\right] \tag{7}$$

$$\frac{\tau_{22}}{\rho} = 2\nu_l \left[\frac{1}{h_2}\frac{\partial \bar{v}}{\partial \eta} + \frac{\bar{u}}{h_1 h_2}\frac{\partial h_2}{\partial \xi}\right] \tag{8}$$

$$\frac{\tau_{12}}{\rho} = \frac{\tau_{21}}{\rho} = \nu_l \left[\frac{h_2}{h_1}\frac{\partial}{\partial \xi}\left(\frac{\bar{v}}{h_2}\right) + \frac{h_1}{h_2}\frac{\partial}{\partial \eta}\left(\frac{\bar{u}}{h_1}\right)\right] \tag{9}$$

where ξ and η = orthogonal curvilinear coordinates in streamwise axis and transverse axis, respectively; h_1 and h_2 = metric coefficients in ξ- and η-directions, respectively; u = ξ-component of velocity; v = η-component of velocity; ρ = fluid density; d = water depth; g = gravitational acceleration; z_b = bed elevation; and τ_{ij} = shear stress acting on the face perpendicular to the i-axis and acting in the direction of the j-axis; τ_{s_i} and τ_{b_i} = ith direction components of free-surface and bed-shear stresses, respectively; $T_{i,j}$ = integrated effective stress; ν_l = laminar kinematic viscosity; overbar ($\bar{}$) = time average; double overbar ($\bar{\bar{}}$) = depth average; prime ($'$) = fluctuating component; and subscripts s and b indicate the dependent variables at the water surface and channel bed, respectively.

The shear stress on the free water surface (caused by the wind) has little significance compared with the bed-shear stress and can be neglected; that is

$$\tau_{s_1} = \tau_{s_2} = 0 \tag{10}$$

The components of the bed-shear stress in the ξ- and η-directions can be written as follows:

$$\tau_{b_1} = C_f \rho \bar{\bar{u}}(\bar{\bar{u}}^2 + \bar{\bar{v}}^2)^{1/2} \tag{11}$$

$$\tau_{b_2} = C_f \rho \bar{\bar{v}}(\bar{\bar{u}}^2 + \bar{\bar{v}}^2)^{1/2} \tag{12}$$

where $C_f = g/c^2$ = friction factor; and c = Chézy factor.

Integrated Effective Stresses

Eqs. (4)–(6) are the integrated effective stresses that act tangentially on the sides of a fluid element. Each of them consists of laminar viscous stress, turbulent stress, and dispersion stress due to depth-averaging. In this study, the depth-averaged turbulent stress is computed using Boussinesq's eddy viscosity concept. It is assumed to be proportional to gradients of the depth-averaged velocities like the laminar viscous stress. The combination of laminar and turbulent kinematic viscosity ν_{l+t}, substituting for ν_l in (7)–(9), can be expressed as

$$\nu_{l+t} = \nu_l + \nu_t \tag{13}$$

where $\nu_t = \kappa u_* d/6$ (Falconer 1980) is used; $u_* = (\tau_b/\rho)^{1/2}$ = shear velocity; and κ = van Kármán's constant (about 0.4).

As mentioned before, the secondary flow in channel bends is caused by the local imbalance between the centrifugal forces and the transverse pressure forces generated by superelevation of the water surface. The vertical distributions of the velocity are no longer uniform. In this model, the velocity profiles in the streamwise and transverse directions proposed by de Vriend (1977) are adopted

$$\bar{u} = \bar{\bar{u}}\left[1 + \frac{\sqrt{g}}{\kappa c} + \frac{\sqrt{g}}{\kappa c}\ln \zeta\right] = \bar{\bar{u}} f_m(\zeta) \tag{14}$$

$$\bar{v} = \bar{\bar{v}} f_m(\zeta) + \frac{\bar{\bar{u}}\bar{\bar{d}}}{\kappa^2 r}\left[2F_1(\zeta) + \frac{\sqrt{g}}{\kappa c} F_2(\zeta) - 2\left(1 - \frac{\sqrt{g}}{\kappa c}\right)\cdot f_m(\zeta)\right]$$

J. Hydraul. Eng. 1999.125:1097-1108.

(15)

in which

$$f_m(\zeta) = 1 + \frac{\sqrt{g}}{\kappa C} + \frac{\sqrt{g}}{\kappa C} \ln \zeta \tag{16}$$

$$F_1(\zeta) = \int_0^1 \frac{\ln \zeta}{\zeta - 1}\, d\zeta \tag{17}$$

$$F_2(\zeta) = \int_0^1 \frac{\ln^2 \zeta}{\zeta - 1}\, d\zeta \tag{18}$$

where $\zeta = (z - z_b)/d$ = dimensionless distance from the bed; and r = radius of curvature.

According to (14) and (15), the main velocity profile is assumed to have a logarithmic distribution, and the transverse velocity profile is a combination of a logarithmic distribution and a nonlinear distribution of the secondary flow. It is obvious that only the secondary flow due to the curvature of the bend is considered in the formulation of the transverse velocity profile. Such consideration of transverse secondary flow is a main factor to shift the streamwise momentum from the inner region of a bend toward the outer region and to increase the main velocity near the outer bank. In addition, the effect of the secondary flow on the streamwise velocity profile is neglected, and these velocity profiles, used in the model, are inadequate for a reverse secondary eddy that occurred near the surface at the outer bank. After including the velocity profiles shown in (14) and (15), the dispersion stress terms can be derived as follows. The first term (DSXX) indicates that the integration of the products of the discrepancy between the mean and the true velocity distributions in the streamwise direction

$$\rho \int_{z_b}^{z_s} (\bar{u} - \bar{\bar{u}})^2\, dz = \rho \int_{z_b}^{z_s} \bar{\bar{u}}^2 \left[1 + \frac{\sqrt{g}}{\kappa C} + \frac{\sqrt{g}}{\kappa C} \ln\left(\frac{z - z_b}{d}\right) - 1\right]^2 dz = \rho \int_0^1 \bar{\bar{u}}^2 d \cdot \left[\frac{\sqrt{g}}{\kappa C} + \frac{\sqrt{g}}{\kappa C} \ln(\zeta)\right]^2 d\zeta = \rho \bar{\bar{u}}^2 d \left(\frac{\sqrt{g}}{\kappa C}\right)^2 = \text{DSXX} \tag{19}$$

The second term (DSYY) indicates that the integration of the products of velocity discrepancy in the transverse direction.

$$\rho \int_{z_b}^{z_s} (\bar{v} - \bar{\bar{v}})^2\, dz = \rho d \int_0^1 \left\{\bar{v}\left[\frac{\sqrt{g}}{\kappa C} + \frac{\sqrt{g}}{\kappa C} \ln \zeta\right] + \frac{\bar{\bar{u}} d}{\kappa^2 r}\left[2F_1(\zeta) + \frac{\sqrt{g}}{\kappa C} F_2(\zeta) - 2\left(1 - \frac{\sqrt{g}}{\kappa C}\right) \cdot f_m(\zeta)\right]\right\}^2 dz = \rho \left[\bar{\bar{v}}^2 d \left(\frac{\sqrt{g}}{\kappa C}\right)^2 + \frac{2\bar{\bar{u}}\bar{\bar{v}} d^2}{\kappa^2 r} \frac{\sqrt{g}}{\kappa C} \cdot FF1 + \frac{\bar{\bar{u}}^2 d^3}{\kappa^4 r^2} \cdot FF2\right] = \text{DSYY} \tag{20}$$

The third term (DSXY) indicates that the integration of the products of velocity discrepancy in the streamwise direction and that in the transverse direction

$$\rho \int_{z_b}^{z_s} (\bar{u} - \bar{\bar{u}})(\bar{v} - \bar{\bar{v}})\, dz = \rho d \int_0^1 \left\{\bar{u}\left[\frac{\sqrt{g}}{\kappa C} + \frac{\sqrt{g}}{\kappa C} \ln \zeta\right]\right\} \cdot \left\{\bar{v}\left[\frac{\sqrt{g}}{\kappa C} + \frac{\sqrt{g}}{\kappa C} \ln \zeta\right] + \frac{\bar{\bar{u}} d}{\kappa^2 r}\left[2F_1(\zeta) + \frac{\sqrt{g}}{\kappa C} F_2(\zeta) - 2\left(1 - \frac{\sqrt{g}}{\kappa C}\right) \cdot f_m(\zeta)\right]\right\} dz = \rho \left[\bar{\bar{u}}\bar{\bar{v}} d \left(\frac{\sqrt{g}}{\kappa C}\right)^2 + \frac{\bar{\bar{u}}^2 d^2}{\kappa^2 r} \frac{\sqrt{g}}{\kappa C} \cdot FF1\right] = \text{DSXY} \tag{21}$$

where

$$FF1 = \int_0^1 (1 + \ln \zeta)\left[2F_1(\zeta) + \frac{\sqrt{g}}{\kappa C} F_2(\zeta) - 2\left(1 - \frac{\sqrt{g}}{\kappa C}\right) \cdot f_m(\zeta)\right] d\zeta \tag{22}$$

$$FF2 = \int_0^1 \left[2F_1(\zeta) + \frac{\sqrt{g}}{\kappa C} F_2(\zeta) - 2\left(1 - \frac{\sqrt{g}}{\kappa C}\right) \cdot f_m(\zeta)\right]^2 d\zeta \tag{23}$$

Note that (22) and (23) can be integrated numerically by using the trapezoidal rule.

NUMERICAL ALGORITHM

Two-Step Split-Operator Approach

The present model used a two-step split-operator approach proposed by Lien et al. (1999) for solving the governing equations. The key feature of this method is to solve the momentum equations in two steps. The first step (dispersion step) is to compute the provisional velocity in the momentum equations without considering the pressure gradient and bed friction. The second step (propagation step) is to correct the provisional velocity by considering a divergence-free velocity field including the effect of the pressure gradient and bed friction. They are expressed sequentially in the vector form as follows:

Dispersion step

$$\left(\frac{\partial \mathbf{V}}{\partial t}\right)^d = -(\mathbf{V} \cdot \nabla)\mathbf{V}^n + \frac{1}{\rho} \nabla \cdot T^n \tag{24}$$

Propagation step

$$\left(\frac{\partial \mathbf{V}}{\partial t}\right)^{n+1} - \left(\frac{\partial \mathbf{V}}{\partial t}\right)^d = -g\nabla(z_b + d)^{n+1} - \frac{\tau_{b_i}}{\rho d} \tag{25}$$

$$\nabla \cdot \mathbf{V}^{n+1} = 0 \tag{26}$$

After proceeding with depth-averaging and dropping the double overbar ($\bar{\bar{}}$) for simplification, one can derive the difference form of (28)–(30) in the orthogonal curvilinear coordinate system as follows:

Dispersion step

$$\frac{u^d - u^n}{\Delta t} = -\frac{u^n}{h_1} \cdot \left(\frac{\Delta u^n}{\Delta \xi}\right) - \frac{v^n}{h_2} \cdot \left(\frac{\Delta u^n}{\Delta \eta}\right) - \frac{1}{h_1 h_2} \cdot \left[\frac{\Delta h_1}{\Delta \eta} u^n v^n - \frac{\Delta h_2}{\Delta \xi} (v^n)^2\right] + \frac{1}{\rho h_1 h_2 d} \frac{\Delta(h_2 T_{11}^n)}{\Delta \xi} + \frac{1}{\rho h_1 h_2 d} \frac{\Delta(h_1 T_{12}^n)}{\Delta \eta} + \frac{1}{\rho h_1 h_2 d} \frac{\Delta h_1}{\Delta \eta} T_{12}^n - \frac{1}{\rho h_1 h_2 d} \frac{\Delta h_2}{\Delta \xi} T_{22}^n + \frac{1}{\rho h_1 h_2 d}\left[-(h_2 \tau_{11})_s^n \frac{\Delta z_s}{\Delta \xi} + (h_2 \tau_{11})_b^n \frac{\Delta z_b}{\Delta \xi} - (h_1 \tau_{12})_s^n \frac{\Delta z_s}{\Delta \eta} + (h_1 \tau_{12})_b^n \frac{\Delta z_b}{\Delta \eta}\right] \tag{27}$$

Similarly, the difference form of velocity component in the η-direction can be derived from (3) as follows:

J. Hydraul. Eng. 1999.125:1097-1108.

Propagation step

$$\frac{u^{n+1} - u^d}{\Delta t} = -\frac{g}{h_1}\left[\frac{\partial}{\partial \xi}(z_b + d)^{n+1}\right] - \frac{C_f^n u^{n+1}\sqrt{(u^d)^2 + (v^d)^2}}{d^n} \tag{28}$$

$$h_1 h_2 \frac{d^{n+1} - d^n}{\Delta t} + \frac{\partial}{\partial \xi}(h_2 u^{n+1} d^{n+1}) + \frac{\partial}{\partial \eta}(h_1 v^{n+1} d^{n+1}) = 0 \tag{29}$$

The difference form of velocity component in the η-direction in the propagation step is similar to (28) in which u^d denotes the provisional velocities; superscript n denotes the known variables at time step n; and superscript $n + 1$ denotes the unknown variables at time step $n + 1$.

The expression of velocity at time step $n + 1$ can be rearranged from (28) as

$$u^{n+1} = \frac{1}{C_\tau} u^d - \frac{g\Delta t}{C_\tau h_1}\left[\frac{\partial}{\partial \xi}(z_b + d)^{n+1}\right] \tag{30}$$

where

$$C_\tau = 1 + \Delta t \frac{C_f^n \sqrt{(u^d)^2 + (v^d)^2}}{d^n} \tag{31}$$

Using the first-order Taylor-series expansion term for depth d^{n+1}, one can easily obtain the linearized expression of (30) as

$$(h_2 u d)^{n+1} = \alpha_1 \frac{\partial \Delta d}{\partial \xi} + \beta_1 \Delta d + \gamma_1 \tag{32}$$

where

$$\alpha_1 = -\frac{h_2 g \Delta t}{C_\tau h_1} d^n; \quad \beta_1 = \frac{h_2}{C_\tau} u^d - \frac{h_2 g \Delta t}{C_\tau h_1}\left[\frac{\partial z_b^{n+1}}{\partial \xi} + \frac{\partial d^n}{\partial \xi}\right] \tag{33a,b}$$

$$\gamma_1 = \beta_1 d^n \tag{33c}$$

Similarly, $(h_2 v d)^{n+1}$ is similar to (32). Substituting (32) into (29) leads to

$$h_1 h_2 \frac{\Delta d}{\Delta t} + \frac{\partial}{\partial \xi}\left(\alpha_1 \frac{\partial \Delta d}{\partial \xi} + \beta_1 \Delta d + \gamma_1\right) + \frac{\partial}{\partial \eta}\left(\alpha_2 \frac{\partial \Delta d}{\partial \eta} + \beta_2 \Delta d + \gamma_2\right) = 0 \tag{34}$$

where $\Delta d = d^{n+1} - d^n$ = increment of depth.

Boundary Conditions

The boundary conditions needed for (34) are usually the discharge hydrograph per unit width at the upstream end and water surface elevation at the downstream end. These types of boundary conditions are easily transformed into the function of the depth-increment variables in (34) (Lien et al. 1999).

At solid boundaries, the law of the wall is applied outside the viscous sublayer and transition layer, in the range of $30 < y^+ < 100$, in which $y^+ = y_w u_* / v$; and y_w = distance between the first computational grid point adjacent to the wall and the wall itself. Within the wall region, the universal law of the wall is applied as

$$u^+ = \frac{1}{\kappa} \ln(Ey^+) \tag{35}$$

where $u^+ = u_w / u_*$; u_w = depth-averaged resultant velocity near the wall; and E = roughness parameter = 9.0. On the basis of law of the wall, a so-called wall function (Rastogi and Rodi 1978) is formulated, which links the near-wall velocities. Using the logarithmic velocity law given by (35) and the expression for wall shear stress, τ_w ($=\rho u_*^2$) can be expressed as (Biglari and Sturm 1998)

$$\frac{\tau_w}{\rho} = \frac{\kappa u_* u_w}{\ln(Ey^+)} \tag{36}$$

The above wall shear stress is used as the wall boundary condition and is substituted into the momentum equation in the wall region to solve for the velocity component parallel to the wall.

VERIFICATION AND ANALYSIS

To verify the capabilities of the proposed model, two sets of experimental data on bend flow conducted by de Vriend and Koch (1977) and Rozovskii (1961) are adopted herein. Data regarding the channel dimensions and flow conditions are summarized in Table 1. Note that the two channels in Table 1 belong to mildly curved and sharply curved channels, respectively. Because the explicit scheme is used in the dispersion step, the stability of the solution is determined from the Courant-Friedrichs-Lewy (CFL) condition

$$\text{CFL} = \max_{i,j}\left[\left(\frac{|u_{i,j}|}{\Delta x_1} + \frac{|v_{i,j}|}{\Delta y_j}\right)\Delta t\right] < 1 \tag{37}$$

With regard to the model's convergence, the following criteria should be satisfied:

$$\max[(\Psi_{i,j}^{n+1} - \Psi_{i,j}^n)/\Psi_{i,j}^n] \le 1.0 \times 10^{-5} \tag{38}$$

where Ψ could stand for $\bar{\bar{u}}$, $\bar{\bar{v}}$, or d. For the unsteady-state case, calculation will not stop until the specified time period is reached.

Flow in Mildly Curved Channel

In de Vriend and Koch's mild-bend flow equipment experiment, the channel consisted of a 39-m-long straight section followed by a 90° bend with a radius of curvature of 50 m. The channel cross section was rectangular, and the width was 6 m. The channel bed was horizontal in the straight part and had a longitudinal slope of 3×10^{-4} in the curved part. The discharge given from the upstream end of the channel was 0.61 m^3/s; the average velocity UM was about 0.4 m/s, and the average flow depth was 0.25 m.

A mesh of 103×35, a time interval $\Delta t = 1.0$ s, and the no-slip boundary at the banks were used in the numerical simulation. The simulation reach covered a 23-m-long straight channel before the entrance of the bend to the tailgate at the end of the channel. The upstream boundary condition was the inflow discharge per unit width, and the downstream boundary condition was the measured flow depth. It can be observed from the experiment that the main velocity near the outer bank

TABLE 1. Channel Dimensions and Flow Conditions in Experiments of de Vriend and Koch (1977) and Rozovskii (1961)

Experimenter (1)	Discharge Q (m^3/s) (2)	Depth d (m) (3)	Width B (m) (4)	Bend radius R_c (m) (5)	B/R_c (6)	θ (degrees) (7)	Chézy factor c ($m^{1/2}/s$) (8)	Froude number F (9)	Reynold's number R (10)	Dean's number $R\sqrt{d/R_c}$ (11)	Grid number (12)	Time step Δt (s) (13)
de Vriend and Koch (1977)	0.610	0.25	6	50	0.12	90	70	0.26	9.2×10^4	6,505	103×35	1.0
Rozovskii (1961)	0.0123	0.058	0.8	0.8	1.0	180	60	0.35	1.4×10^3	377	61×43	0.05

J. Hydraul. Eng. 1999.125:1097-1108.

increases along the bend and becomes greater than that near the inner bank due to the transverse convection of streamwise momentum along the bend caused by the secondary flow.

Fig. 1(a) shows the velocity redistribution across the channel width along the bend without considering the dispersion stresses. The simulated results are consistent with the potential theory by which the velocity is inversely proportional to the radius of the curvature. Hence, the flow velocity along the channel bend is higher in the inner-bank region than that in the outer-bank region, as clearly shown in Fig. 1(a). If the dispersion stresses are included in the bend-flow simulation, they act as sink or source in the momentum equation, which cause the transverse convection of momentum to shift from the inner bank to the outer bank (Kalkwijk and de Vriend 1980; de Vriend 1981). Fig. 1(b) shows the simulated results with dispersion stresses, which clearly demonstrate a shift of the maximum main velocity along the channel bend from the inner-bank region toward the outer-bank region. Fig. 2 shows the variation of velocity ratios U/UM across the dimensionless channel width $[(R - R_i)B]$ obtained from the present model, the measured value, and Yeh's moment-of-momentum model, where U is the depth-averaged velocity, and R_i is the radius of curvature of the inner bank. It can be observed from Fig. 2 that the velocity becomes lower near the inner bank and higher near the outer bank starting from the $\theta = 27.5°$ section. This phenomenon is becoming more distinguishing as the flow moves further downstream. The computed results with the effect of secondary flow have good agreement with the measured data. It clearly shows that the transverse convection of momentum shifting from the inner bank to the outer bank is due to the consideration of dispersion stress terms in the momentum equations. Fig. 3 shows the corresponding dimensionless depth ratio $(Zs\text{-}Zsm)/d$ against the dimensionless channel width, where Zsm is the mean water surface elevation across the channel width. The difference between the simulated results with and without secondary flow is not significant because the secondary-flow effect in the mild bend is weak.

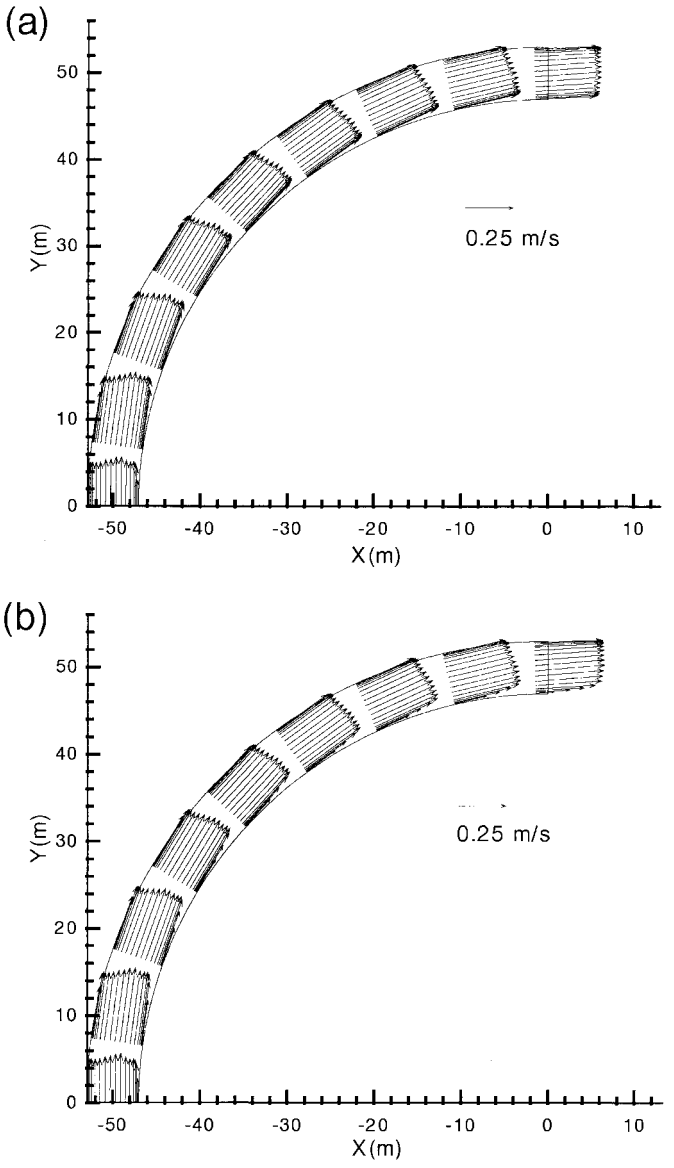

FIG. 1. Velocity Redistribution for de Vriend and Koch's Simulation: (a) without Secondary Flow; (b) with Secondary Flow

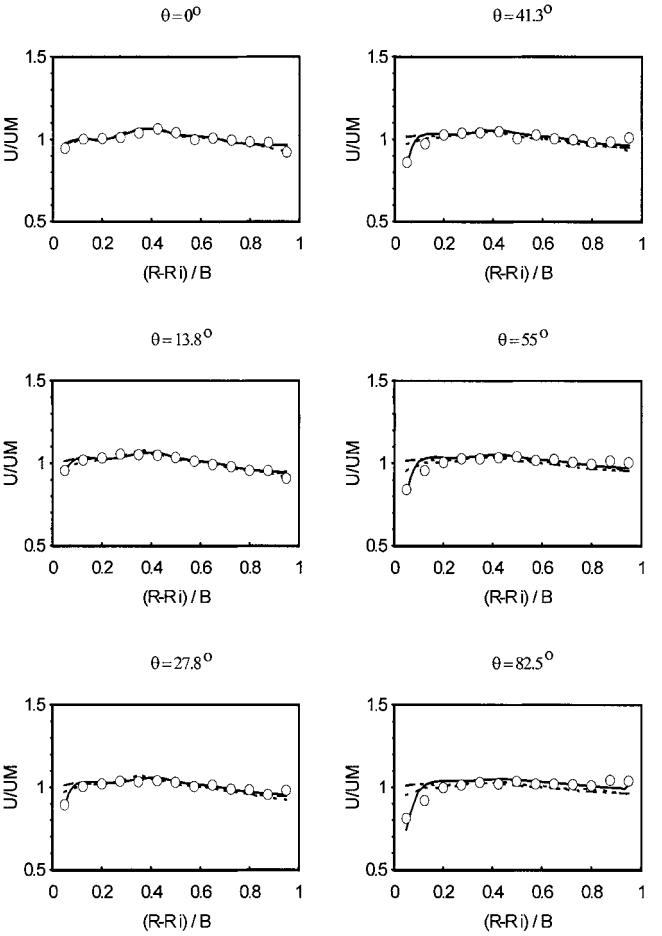

FIG. 2. Velocity Ratio *U/UM* across Dimensionless Channel Width for de Vriend and Koch's Simulation. Measured (○); Computed with Secondary Flow (——); Computed without Secondary Flow (– · · –); and Yeh's Model (1993) (· · · ·)

Flow in Sharply Curved Channel

Rozovskii (1961) constructed a sharp 80° bend channel in which the ratio of width to mean radius of curvature was 1.0. A curve with a width-to-mean radius ratio of 0.4 and more is considered to be sharp and will exhibit highly 3D flow characteristics. The cross section of the bend was rectangular and connected to straight inlet and outlet reaches of the same cross section. The approach channel was 6 m long, and the exit channel was 3 m in length. The entire channel was horizontal. The channel bottom was smooth, and the Chézy coefficient was 60 $m^{1/2}/s$. The Reynolds number was 15,600 and the Froude number was 0.11. The discharge in the channel was 0.0123 m^3/s, and the averaged velocity (UM) was about 0.265 m/s. This set of data was referred to as experiment No. 1 in a series of Rozovskii's bend-flow experiments (1961).

J. Hydraul. Eng. 1999.125:1097-1108.

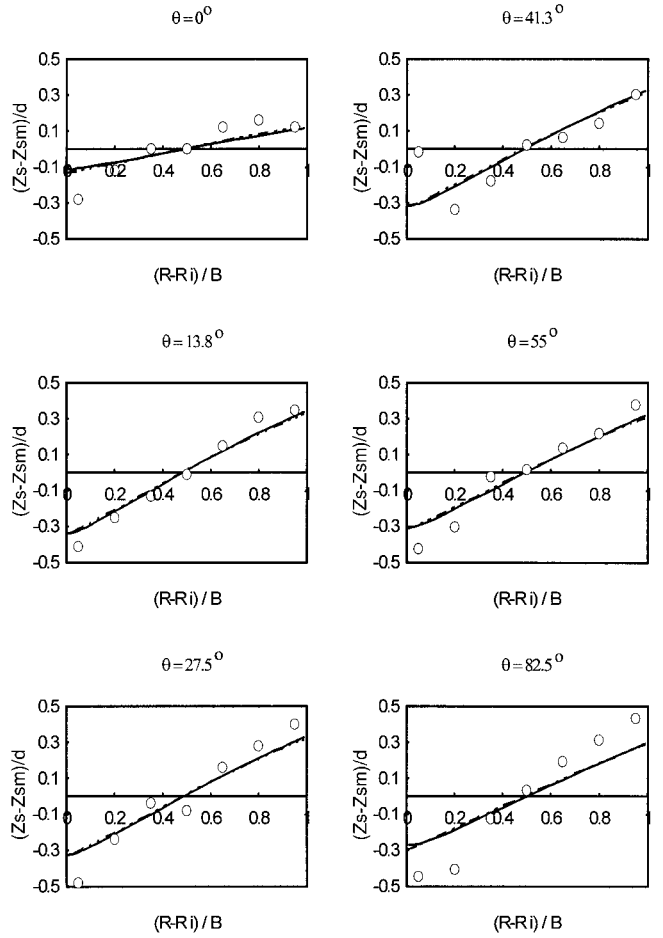

FIG. 3. Depth Ratio (*Zs* = *Zsm*)/*d* across Dimensionless Channel Width for de Vriend and Koch's Simulation. Measured (○); Computed with Secondary Flow (——); and Computed without Secondary Flow (– · · –)

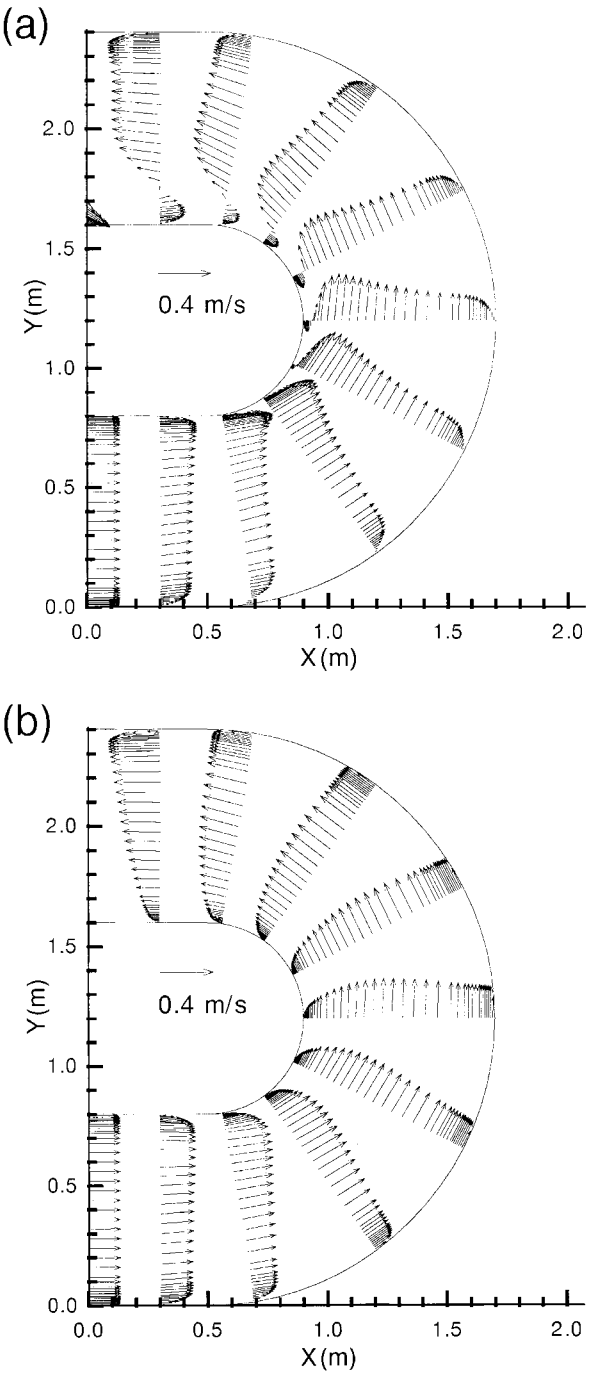

FIG. 4. Velocity Redistribution by Numerical Simulation for Rozovskii's Experiment Using No-Slip Condition: (a) without Secondary Flow; (b) with Secondary Flow

A grid system composed of 61 × 43 nodes and time interval Δt = 0.05 s were used in the numerical simulation. The inlet boundary of inflow discharge was located 0.5 m upstream of the bend, and the outlet boundary of measured flow depth was located 0.5 m downstream of the bend.

By referring to Figs. 4–6, results of numerical simulation using the no-slip and free-slip conditions may be compared. Figs. 4(a and b) show the computed velocity distribution across the channel width without/with the secondary flow effect using the no-slip condition at the banks, respectively. Without considering the secondary flow effect, a recirculation zone near the bend outlet is developed where the flow separates from the inner sidewall. However, in Rozovskii's experiment the flow separation was not observed. The simulated results using the no-slip condition with the secondary flow effect shown in Fig. 4(b) in which the flow separation disappears near the exit of the bend is clearly better than the computed results without considering the secondary flow effect from Fig. 4(a).

Figs. 5(a) and 5(b) show the computed velocity distribution across the channel width using the free-slip condition at the banks without/with the secondary flow effect, respectively. As shown in Fig. 5(a), the velocity at the inner bank becomes larger and that at the outer bank becomes smaller when the flow enters the bend. Such a flow pattern prevails through the entire bend. The simulated streamwise velocity becomes uniform again after a short distance downstream of the bend exit. When considering the secondary flow effect, Fig. 5(b) indicates different velocity distributions after the flow enters the bend. The maximum main velocity at the inner bank with the secondary flow effect is smaller than that without considering the secondary flow effect. Furthermore, Fig. 5(b) shows that the velocity distribution with the secondary flow effect is no longer uniform in the straight channel even after the flow exits the bend. The velocity near the outer-bank region abruptly speeds up, and the corresponding velocity near the inner-bank region decelerates. This phenomenon can be explained by the decline of the transverse slope of the water surface and the release of the remaining additional momentum by the secondary flow effect when the radius of curvature at the bend exit abruptly changes to infinity.

Fig. 6 shows the simulated results of *U*/*UM* across the nondimensional channel width at the different sections. In Fig. 6,

J. Hydraul. Eng. 1999.125:1097-1108.

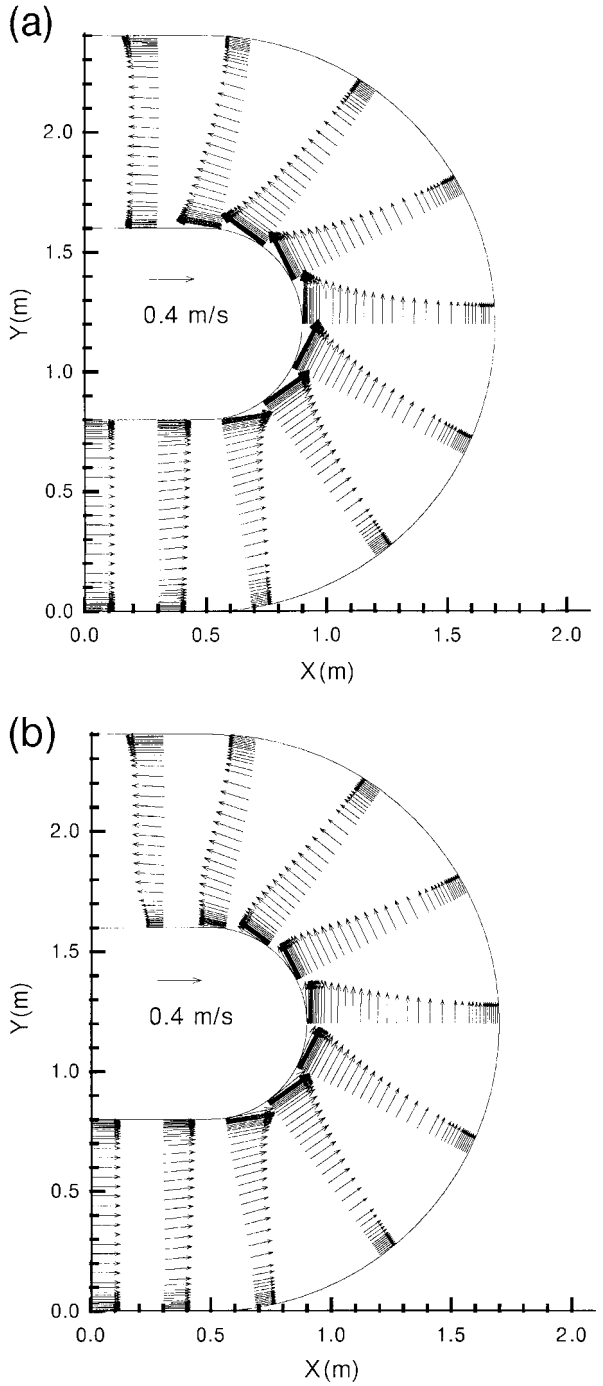

FIG. 5. Velocity Redistribution by Numerical Simulation for Rozovskii's Experiment Using Free-Slip Condition: (a) without Secondary Flow; (b) with Secondary Flow

simulated results from three cases with various conditions are compared with the experimental data, which are no-slip/free-slip with the secondary flow effect cases and free-slip without the secondary flow effect case. Coincidentally, the results for the free-slip case with the secondary flow effect shows better consistency with the experimental data than those for the no-slip case with the secondary flow effect (Molls and Chaudhry 1995) along the curved region of the channel. Nevertheless, the latter case shows the persuasive results at the entrance and the exit of the bend (θ = 0° and 86° sections) but a rather significant deviation from the experimental data from θ = 35° to 143°. The deviation may be because the effect of the no-slip boundary condition on the inner bank is too strong, which may induce the computed velocity near the inner bank to be smaller and that near the outer bank to be greater in compar-

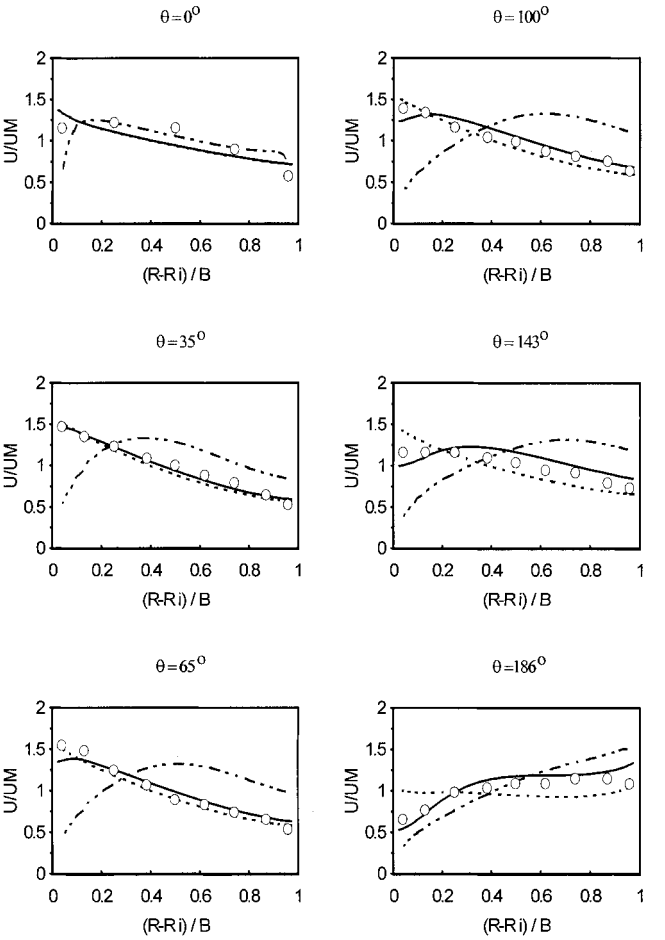

FIG. 6. Velocity Ratio *U*/*UM* across Dimensionless Channel Width for Rozovskii's Simulation. Measured (○); Computed with Secondary Flow (Free-Slip) (——); Computed without Secondary Flow (Free-Slip) (· · · ·); and Computed with Secondary Flow (No-Slip) (– · · –)

ison with the experimental data. It appears that the use of the wall function with the depth-averaged Boussinesq's eddy viscosity, along with the assumption of bed-shear stresses shown in (15) and (16), cannot completely solve the near-wall problems, although it has agreeable results from the flow in the mildly curved channel. In fact, the modeling flow phenomenon near the wall will remain a challenge for flow simulation in years to come. Further research for solving near-wall problems by the depth-averaged model is underway. However, based on previous investigation, one can obviously observe that the secondary flow effect plays the significant role in bend-flow simulation. In the review of the existing depth-averaged bend-flow model, most of the models simulated bend flow using the free-slip condition at the bank. Because the main purpose here is to examine the effect of dispersion stresses, it may be better to avoid the unnecessary complication caused by the no-slip condition. Hence in the following discussion, the results based on the free-slip condition are chosen to compare with the experimental data and the results from Yeh's moment-of-momentum model (1993) and Molls's model (1995), which were also based on the free-slip condition.

Fig. 6 shows that the free-slip case without the secondary flow effect seems to have good agreement with the experimental data from θ = 35° to 100° but have poor agreement from θ = 143° to 185°. It also clearly shows that the velocity distribution pattern across the channel width computed without the secondary flow effect remains almost constant in the bend except near the exit of the bend. However, the experimental data show that the maximum main velocity abruptly shifts to-

J. Hydraul. Eng. 1999.125:1097-1108.

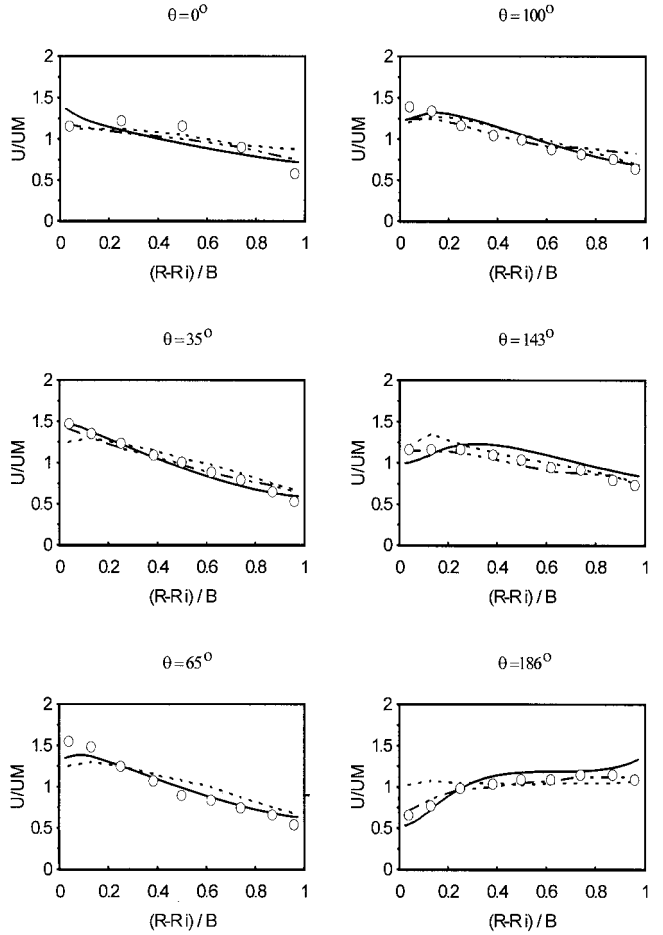

FIG. 7. Velocity Ratio *U*/*UM* across Dimensionless Channel Width for Rozovskii's Simulation. Measured (○); Computed with Secondary Flow (Free-Slip) (——); Yeh's (Free-Slip) Model (1993) (· · · ·); and Leschziner's Model (1979) (– · · –)

ward the outer bank at the θ = 186° section. Such flow phenomenon can be simulated by considering the secondary flow effect. In general, the proposed model has satisfactory performance compared with the experimental data. In the reach between θ = 35° and 186° sections, the experimental data and the simulated results with the secondary flow effect clearly show that, along the curved channel, the velocity near the inner bank is gradually decreasing whereas the velocity near the outer bank is increasing. In the reach between θ = 35° and 100°, there is little difference between measured and computed primary velocity near the inner bank. This may be because the intensity of the secondary flow used in modeling is larger than that from practical flow characteristics in this reach. Fig. 7 shows the ratios of *U*/*UM* across the nondimensional channel width at the various sections. The results obtained from the present model are compared with Yeh's moment-of-momentum model, the 3D model developed by Leschziner and Rodi (1979), and the experimental data. It is expected that the 3D model would perform much better than the 2D models because the flow in the sharply curved bend is highly 3D. Surprisingly, the present model produces similar results to those of the 3D model, particularly near the bend exit. Fig. 8 shows the variations of the sidewall flow depth using free-slip condition with/without secondary flow along the dimensionless channel length [channel length over channel width (i.e., *S*/*B*). It can be seen that, along the bend, the water level rises at the outer bank and falls at the inner bank. Note that, without the secondary flow effect, the water level will be underestimated at the outer bank. Furthermore, the consideration of the secondary flow effect can decrease the slope of superelevation between the inner bank and outer bank as observed in measured data.

Fig. 9 shows the sidewall flow depth in a comparison of the present model (free-slip), the 2D model (free-slip) developed by Molls and Chaudhry (1995), the 3D model, and the experimental data. With the exception of the small deviation at the upstream boundary, the outer-bank predictions with the present model is slightly more accurate than those predicted by 3D and Molls-Chaudhry models. The inner-bank sidewall flow depth is predicted better by the 3D model. For all the models considered, the maximum relative error in the sidewall flow depth occurred along the inner bank. The maximum error of the present model is about 4.5% and occurred at the dimensionless channel length of 1.25. The Molls-Chaudhry model is about 5.5% at the dimensionless channel length of 3.15, and the 3D model is about 2.5% at the dimensionless channel length of 2.4.

In short, the different patterns of velocity distribution across channel width between a mildly curved channel and a sharply curved channel can be clearly seen by a comparison of Figs. 1(b) and 5(b). The maximum main velocity occurred at the outer bank in a mildly curved channel due to the secondary flow effect (de Vriend 1981). In contrast, the maximum main velocity was observed at the inner bank in a sharply curved channel, but it is toward the outer bank after exiting the end of the curved channel. Usually, the large intensity of secondary flow in the sharp bend will increase the transverse convection of momentum causing the maximum main velocity toward the outer bank. On the other hand, as the curve becomes sharper, the free-vortex effect will grow stronger in the bend like the potential flow (de Vriend 1981). Hence, such flow phenomenon in a sharply curved channel may occur because the free-vortex effect is larger than the secondary flow effect. In addition, the CPU time needed for Rozovskii's run is about 1.25 times that of de Vriend and Koch's run.

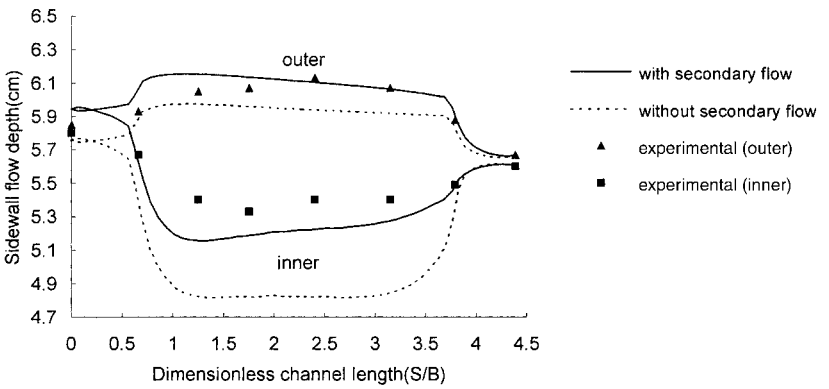

FIG. 8. Sidewall Flow Depth (Free-Slip Cases with/without Secondary-Flow Comparison)

J. Hydraul. Eng. 1999.125:1097-1108.

Examination of Dispersion Stress Terms

The dispersion stresses are important terms to describe the secondary flow effect in bend-flow simulations. The role of dispersion stresses in the simulation of Rozovskii's case is discussed first in the following. Since in Rozovskii's case the channel geometry is a semicircle, the curvilinear coordinate system simply becomes a polar coordinate system. The metric coefficient h_1 is equal to the radius of curvature, and h_2 is equal to unity. Therefore the derivative of h_1 with respect to η (transverse direction) is unity and that of h_2 with respect to ξ (streamwise direction) vanishes, so that in the ξ-direction momentum equation DSXY is two times larger and DSXX and DSYY vanish. Similarly, DSXY vanishes and DSXX and DSYY remain in the η-direction momentum equation. Fig. 10 shows the variation of each dispersion stress components [i.e., DSXX, DSYY, and DSXY in (23)–(25)] in the ξ-direction or η-direction momentum equations at the centerline along the dimensionless channel length. The DSYY is the dominant stress in the bend, which is about seven times larger than DSXX and three times larger than DSXY. In Fig. 10, the dispersion stresses appear to abruptly change near the entrance and exit of the bend. This may not be unexpected because the velocity profile introduced for the computation of the secondary flow effect is considered under the fully developed condition. The developing variation may exist while flow moves through the transition region that is from the straight channel to the bend or near the inflection of the S-curved channel. Fig. 11 shows the variation of some significant forces, including the centrifugal force (CFX), dispersion force ($2 \cdot$DSXY), and bed friction (BFX) in the ξ-direction momentum equation, along the centerline of the channel. It is clear that the dispersion force ($2 \cdot$DSXY) is larger than the bed friction as shown in Fig. 11. This illustrates the importance of dispersion stresses in bend-flow simulations. Fig. 12 shows the variation of some significant forces, including centrifugal force (CFY), dispersion forces (DSXX and DSYY), and bed friction (BFY) in the η-direction momentum equation, along the centerline of the channel. Fig. 12 shows that the centrifugal force is the major force component in the η-direction, DSYY has much less effect, and DSXX and BFY give almost no effect.

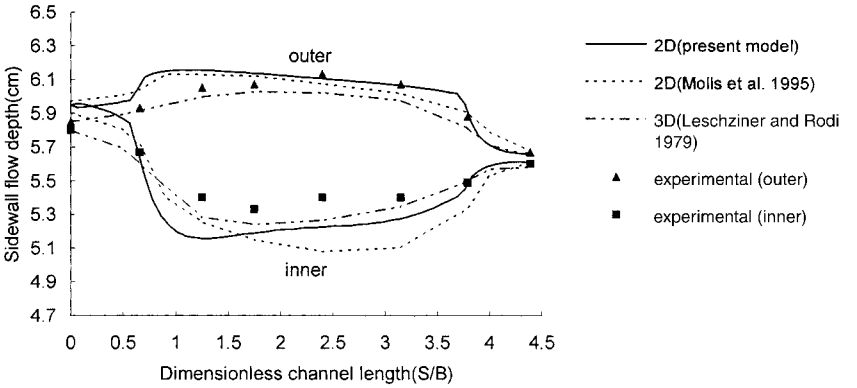

FIG. 9. Sidewall Flow Depth (2D- and 3D-Model Comparison)

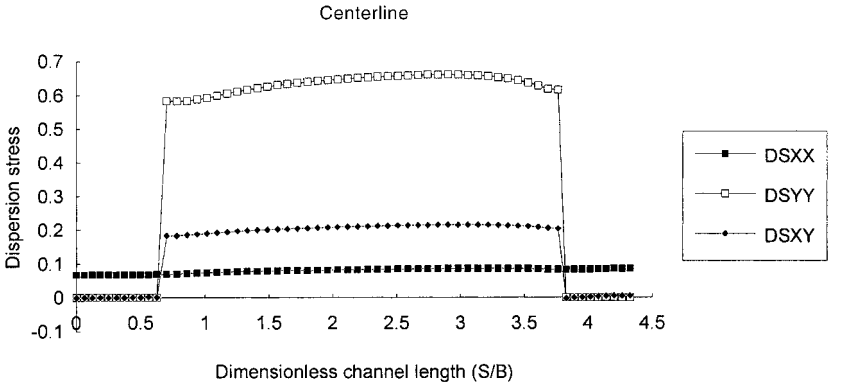

FIG. 10. Variation of Dispersion Stresses along Dimensionless Channel Length for Rozovskii's Simulation

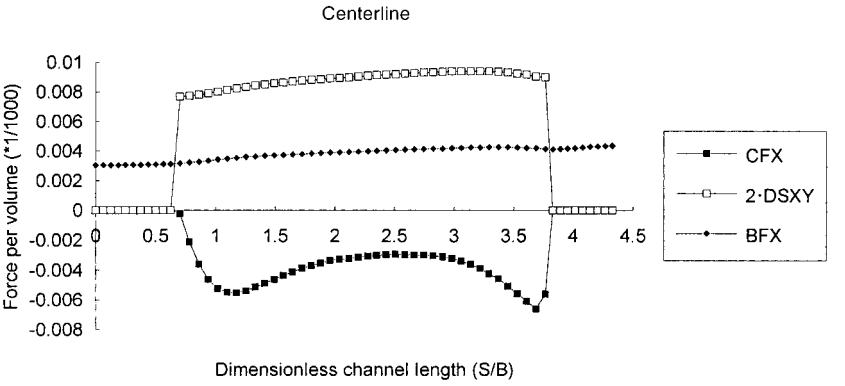

FIG. 11. Variation of Force in ξ-Direction Momentum Equation for Rozovskii's Simulation

J. Hydraul. Eng. 1999.125:1097-1108.

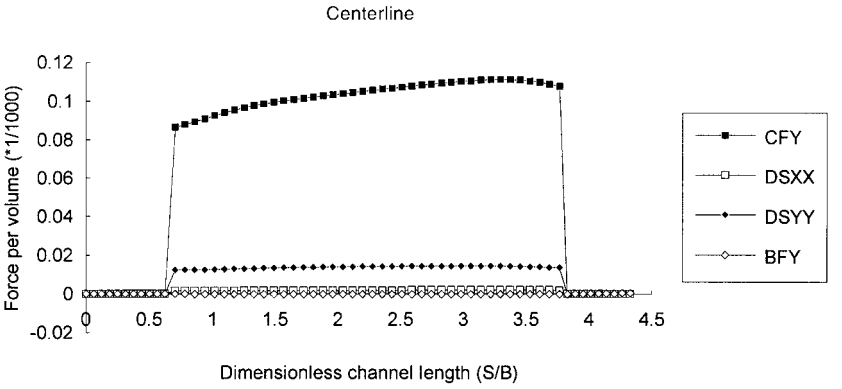

FIG. 12. Variation of Force in η-Direction Momentum Equation for Rozovskii's Simulation

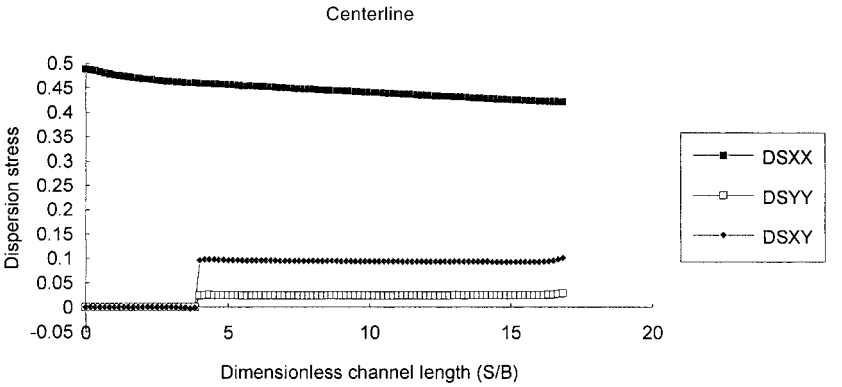

FIG. 13. Variation of Dispersion Stresses for de Vriend and Koch's Simulation

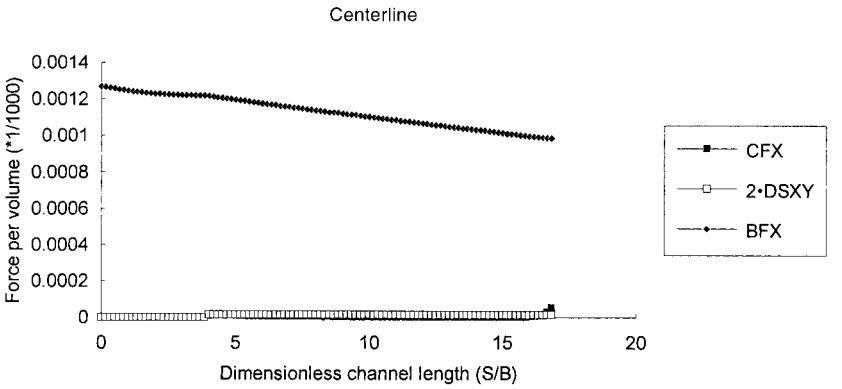

FIG. 14. Variation of Force in ξ-Direction Momentum Equation for de Vriend and Koch's Simulation

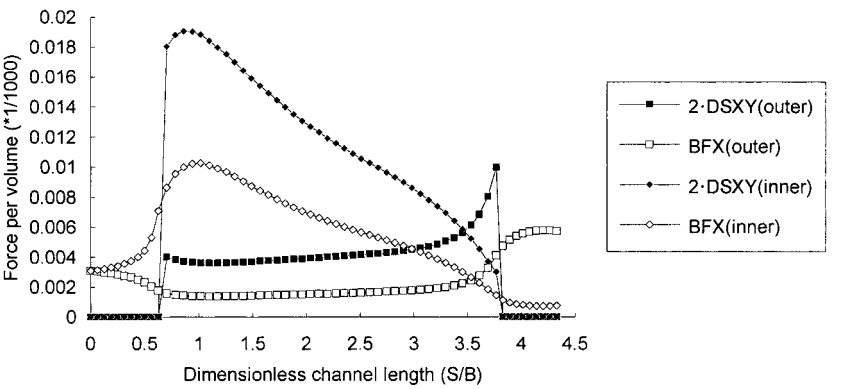

FIG. 15. Comparison of Forces at Outer and Inner Banks for Rozovskii's Simulation

J. Hydraul. Eng. 1999.125:1097-1108.

As for the simulation of de Vriend and Koch's experiment, Figs. 13 and 14, respectively, show the comparisons of variations of dispersion stress terms and significant forces in the ξ-direction along the centerline of the channel. In Fig. 13, it is obvious that the major stress is DSXX, and DSXY and DSYY are much smaller. In a comparison of the results for the mildly curved channel (Fig. 13) and the sharply curved channel (Fig. 10), one can find that the dispersion stresses play the various level of effect to the flow development in the bend. For the mildly curved channel, DSXX is the major stress, and for the sharply curved channel, DSYY becomes the significant one. Furthermore, as observed from Fig 14, the bed friction is the dominant force whereas the centrifugal force and dispersion force are minor. In comparing Figs. 14 and 11, it may lead to the consequence that the corresponding intensity of secondary flow appearing in the sharp bend is stronger than that in the mild bend because the dispersion force ($2 \cdot$DSXY) is the most dominant force in the sharp bend. Fig. 15 shows a comparison of forces between the outer bank and the inner bank in the ξ-direction momentum equation for Rozovskii's simulation. The dispersion force ($2 \cdot$DSXY) near the inner bank decreases rapidly from the beginning of the bend to the end of the curve, whereas at the outer bank it varies gently along the bend but abruptly increases near the end of the curve. This phenomenon may demonstrate the transverse convection of streamwise momentum by the variation of the dispersion force to simulate the secondary flow effect in the bend. The bed friction at the outer and inner banks varies in the same way as the dispersion force.

In summary, dispersion stresses are an important factor that should be considered in bend-flow simulations. They act as sink or source in the momentum equations and contribute to the transverse convection of the momentum. Their relative contributions in the overall secondary flow effect depend on flows in mild or sharp bends.

CONCLUSIONS

This paper presents an unsteady 2D depth-averaged model developed using orthogonal curvilinear coordinate system. The model takes into account vertical velocity profiles in a bend using them to capture the effect of dispersion stress on the floor. Dispersion stress terms serve as a sink or source in the momentum-conservation equations needed to calculate the transverse convection of momentum caused by the secondary flow along a channel bend (Kalkwijk and de Vriend 1980; de Vriend 1981). If the dispersion stress terms are neglected, the government equations reduce to a conventional depth-averaged equation assuming uniform velocity over depth. In other words, the model presented herein should be more applicable for practical application in bend-flow modeling than the conventional depth-averaged models because of its ability to account for the secondary flow effect.

Two sets of experimental bend-flow data, one with mild bends and one with sharp bends, were used to demonstrate the capabilities of the proposed model. The simulated results and experimental data agree well in the case of the mildly curved channel. Although some discrepancies exist between the computed results and the measured data in the sharply curved channel, the computed results show that the secondary flow effect has been properly represented by calculating the dispersion stresses. According to the analysis of the dispersion stress terms, the contribution of each dispersion stress component has been demonstrated for the mildly curved and sharply curved channels. The DSXX is the major stress in the mildly curved channel; however, DSYY becomes the dominant stress in the sharply curved channel. Furthermore, one can observe from the growth and shrinkage of dispersion stress for Rozovskii's simulation along the outer and inner banks, as shown in Fig. 15, that the shift of the streamwise momentum from the inner bank to the outer bank can be clearly realized. In short, the dispersion stresses play an important role in accurately simulating or predicting flow fields in sharp bends as well as in mild bends.

ACKNOWLEDGMENTS

Partial financial support of this study from the National Science Council of Taiwan through Contract NSC-85-2211-E009-034 is greatly appreciated.

APPENDIX I. REFERENCES

Biglari, B., and Sturm, T. W. (1998). ''Numerical modeling of flow around bridge abutments in compound channel.'' *J. Hydr. Engrg.*, ASCE, 124(2), 156–164.

de Vriend, H. J. (1977). ''A mathematical model of steady flow in curved shallow channel.'' *J. Hydr. Res.*, Delft, The Netherlands, 15(1), 37–54.

de Vriend, H. J. (1981). ''Velocity redistribution in curved rectangular channels.'' *J. Fluid Mech.*, Cambridge, U.K., 107, 423–439.

de Vriend, H. J., and Geldof, H. J. (1983). ''Main flow velocity in short and sharply curved river bends.'' *Communications on Hydraulics, Rep. No. 83-6*, Dept. of Civ. Engrg., Delft University of Technology, Delft, The Netherlands.

de Vriend, H. J., and Koch, F. G. (1977). ''Flow of water in a curved open channel with a fixed plan bed.'' *Rep. on Experimental and Theoretical Investigations R675-V M1415, Part I*, Delft University of Technology, Delft, The Netherlands.

Falcon Ascanio, M. (1979). ''Analysis of flow in alluvial channel bends,'' PhD thesis, Dept. Mech. and Hydr., University of Iowa, Iowa City, Iowa.

Jin, Y. C., and Steffler, P. M. (1993). ''Predicting flow in curved open channels by depth-averaged method.'' *J. Hydr. Engrg.*, ASCE, 119(1), 109–124.

Kalkwijk, J. P. T., and de Vriend, H. J. (1980). ''Computation of the flow in shallow river bends.'' *J. Hydr. Res.*, 18(4), 327–342.

Kikkawa, H., Ikeda, S., and Kitagawa, A. (1976). ''Flow and bed topography in curved open channels.'' *J. Hydr. Div.*, ASCE, 102(9), 1327–1342.

Leschziner, M. A., and Rodi, W. (1979). ''Calculation of strongly curved open channel flow.'' *J. Hydr. Div.*, ASCE, 105(10), 1297–1314.

Lien, H. C., Hsieh, T. Y., and Yang, J. C. (1999). ''Use of two-step split-operator approach for 2-D shallow water flow computation.'' *Int. J. Numer. Methods in Fluids*, in press.

Mockmore, C. (1943). ''Flow around bends in stable channels.'' *Trans., ASCE*, 3, 334.

Molls, T., and Chaudhry, M. H. (1995). ''Depth-averaged open-channel flow model.'' *J. Hydr. Engrg.*, ASCE, 121(6), 453–465.

Nagata, T., Hosoda, T., Muramoto, Y., and Rahman, M. M. (1997). ''Development of the numerical model to forecast the channel processes with bank erosion.'' *Proc., 4th Japan-Chinese (Taipei) Joint Seminar on Natural Hazard Mitigation*, 167–176.

Odgaard, A. J. (1989). ''River-meander model. I: Development.'' *J. Hydr. Engrg.*, ASCE, 115(11), 1433–1450.

Rastogi, A. K., and Rodi, W. (1987). ''Predictions of heat and mass transfer in open channels.'' *J. Hydr. Engrg.*, ASCE, 104(3), 397–420.

Rozovskii, I. L. (1961). *Flow of water in bends of open channels*. The Israel Program for Scientific Translations, Jerusalem.

Shimizu, Y., Yamaguchi, H., and Itakura, T. (1990). ''Three-dimensional computations of flow and bed deformation.'' *J. Hydr. Engrg.*, ASCE, 116(9), 1090–1108.

Shukhry, A. (1949). ''Flow around bends in an open flume.'' *J. Hydr. Div.*, ASCE, 75, 713.

Sinha, S. K., Sotiropoulos, F., and Odgaard, A. J. (1998). ''Three-dimensional numerical model for flow through natural rivers.'' *J. Hydr. Engrg.*, ASCE, 124(1), 13–24.

Thompson, J. (1876). ''On the origin and winding of rivers in alluvial plains, with remarks on flow around bends in pipes.'' *Proc., Royal Soc.*, London, 25, 5.

Yeh, K. C., and Kennedy, J. F. (1993). ''Moment model of nonuniform channel-bend flow. I: Fixed beds.'' *J. Hydr. Engrg.*, ASCE, 119(7), 776–795.

Yen, B. C. (1965). ''Characteristics of subcritical flow in a meandering channel,'' PhD thesis, University of Iowa, Iowa City, Iowa.

Yen, C. L., and Ho, S. Y. (1990). ''Bed evolution of channel bends.'' *J. Hydr. Engrg.*, ASCE, 116(4), 544–562.

Zimmermann, C., and Kennedy, J. F. (1978). ''Transverse bed slopes in curved alluvial stream.'' *J. Hydr. Div.*, ASCE, 104(1), 33–48.

J. Hydraul. Eng. 1999.125:1097-1108.

APPENDIX II. NOTATION

The following symbols are used in this paper:

$C_f = g/c^2$ = friction factor;
c = Chézy factor;
DSXX = dispersion stress as shown in Eq. (19);
DSXY = dispersion stress as shown in Eq. (21);
DSYY = dispersion stress as shown in Eq. (20);
d = water depth;
E = roughness parameter;
$\mathbf{F}$ = body force;
g = gravitational acceleration;
h_1, h_2 = metric coefficients in ξ and η directions, respectively;
P = pressure;
r = radius of curvature;
$T_{i,j}$ = integrated effective stress;
t = time;
u = ξ component of velocity;
u_w = velocity near wall;
u_* = shear velocity;
v = η component of velocity;
z_b = bed elevation;
$\zeta = (z - z_b)/d$ = dimensionless distance from bed;
κ = von Kármán's constant (about 0.4);
ν_l = laminar kinematic viscosity;
ν_t = turbulent kinematic viscosity;
ρ = fluid density;
τ_{ij} = shear stress acting on face perpendicular to i-axis and acting in direction of j-axis;
τ_{s_i}, τ_{b_i} = ith direction components of free-surface and bed-shear stress, respectively; and
τ_w = wall shear stress.

Superscript

d = provisional variable in dispersion step;
n = known variables at time level (n);
$n + 1$ = unknown variables at time level ($n + 1$);
$\bar{(\ )}$ = time average;
$\tilde{(\ )}$ = depth average; and
$(')$ = fluctuating component.

Subscripts

b = dependent variables at channel bed; and
s = dependent variables at water surface.

J. Hydraul. Eng. 1999.125:1097-1108.